The Astrophysical Journal, 854:59 (11pp), 2018 February 10 https://doi.org/10.3847/1538-4357/aaa4f8
© 2018. The American Astronomical Society. All rights reserved.

# Using Cross Entropy Optimization to Model Active Galactic Nuclei Light Curves from VLBA MOJAVE Images

R. P. Vitoriano[1] and L. C. L. Botti[1,2,3]
[1] CRAAM, Center for Radio Astronomy and Astrophysics Mackenzie, Engineering School, Mackenzie Presbyterian University, Rua da Consolação, 896, São Paulo, SP, 01302-907, Brazil
[2] DAS/CEA/INPE/MCTIC, National Institute for Space Research, Av. dos Astronautas, 1758, São José do Campos, SP, 12227-010, Brazil
[3] ROI/INPE, Itapetinga Radio Observatory, Estrada do Mackenzie S/N, Atibaia, SP, 12950-570, Brazil
*Received 2017 June 12; revised 2017 December 30; accepted 2018 January 2; published 2018 February 12*

## Abstract

We present in this article a new method to derive the observed properties of outbursts in relativistic jets. We use the VLBI MOJAVE maps to obtain the light curves, based on the principle that the variability of extragalactic sources, in this case 3C 279 and 4C +29.45, should appear in high resolution observations since 1996 until 2016. The use of the cross entropy method (CE) can accurately determine the ranges of parameters for a sequence of outbursts based on the shock-wave model, where the decay/rise timescale ratio has a small spread and the use of a unique index 1.3 generates a good fit modeled by functions of outbursts and by the model of the three stages. By the CE method, one can automatically get the start epochs as well as the occurrence of rise and decline times of the outbursts in the light curves. The values found are in agreement with the power-law distribution of energy, which shows that the cooling of electrons is a predominant process during the initial phase of the shock model evolution. The results of the decomposition show that the outbursts match the VLBI components observed in jets in addition to showing strong evidence of the peaks in the frequencies of 15.3 GHz. With this, we can model the shock waves with reference to the distance at the core of AGN to obtain the Doppler factor and the Lorentz factor.

*Key words:* galaxies: active – galaxies: jets – galaxies: nuclei – methods: statistical – radio continuum: galaxies – techniques: interferometric

## 1. Introduction

The radio observations obtained from the MOJAVE (2 cm Survey; Lister et al. 2009b), *FERMI*-LAT (Hayashida et al. 2015), and OVRO 40 m telescope monitoring program (Richards et al. 2011) show evidence of prominent structures or outbursts, propagating from high to low frequencies. Modeling the variability of blazars has been the subject of several studies. A general form of understanding the outbursts was made by Marscher & Gear (1985). Valtaoja et al. (1988) attempted to separate the quiescent from the flaring flux through multiwavelength flux density curves (several frequencies from 4.8 to 90 GHz), where the authors examined the spectrum of each source at periods of minimum flux density between outbursts (what they considered as the constant flux density of the jet) and a recent work (Liodakis et al. 2017) presented a bimodal radio variability through the OVRO 40 m telescope. In this work, we will demonstrate a similar behavior for the optically violent variable (OVV) blazar 3C 279 and the blazar 4C +29.45. An innovative method in this work is the use of a statistical accuracy algorithm, called cross entropy (CE; Rubinstein 1997), where it is possible to infer details of the behavior of light curves. The peaks of outbursts observed in the light curves at 4.8, 8.0, and 14.5 GHz (UMRAO Database), 1.7, 22, 37, 90, 150, 230, and 375 GHz (Lindfors et al. 2006) show the individual outbursts as a sum of smaller peaks decomposed by the shock-wave model. With the CE method, we aim to determine the possibility of detection of components in the first approximation, due to the fact that the imposition of a fixed number of outbursts determines a single best fit for a light curve. In this work, we started with 24 up to 33 outbursts. With this incremental coverage, it is possible to estimate the number of such events. In this article, only the results for 33 outbursts will be shown. It is not the goal of this research to discover a definitive number of outbursts, due to the fact that the shock-wave model is complex and faces a large-scale approach; however, we can introduce an incremental model to assume a more detailed formation. During the decomposition of 3C 279 (Lindfors et al. 2006) an amount of 15 outbursts was estimated for the period from 1989 until 1998. In this way, we include in this work about 33 outbursts, assuming that a number of similar occurrences should happen during the period from 1995 until 2016. Türler et al. (1999a) also demonstrated the behavior of a light curve as a shock-wave sequence, where it was imposed that all individual outbursts are self-similar, in the sense that all have the same evolution pattern, i.e., the same shape of the surface in ($S$, $\nu$, $t$) space.

Another object shown in this work is 1156 + 295 (4C +29.45), which also has VLBI maps available in the MOJAVE, whose periods of observation are between 1995 July 04 and 2012 February 11. For this object, we use 24 outbursts. In Hovatta et al. (2009), the 1156 + 295 flux curve was decomposed into exponential outbursts at 22 GHz. The method of approach and decomposition of the outbursts for this object follow the same standards as described for 3C 279.

### 1.1. Properties of Blazar 3C 279

3C 279 (1253-055) is among the best studied blazars, it is detected in all accessible spectral bands, revealing highly variable emission. It consistently shows strong $\gamma$-ray emission, already clearly detected with the EGRET instrument on the Compton Gamma Ray Observatory (Hartman et al. 1992). The object, at $z = 0.536$ (Lynds et al. 1965), is associated with a luminous flat spectrum radio quasar with prominent broad emission lines. Optical and UV observations in the low-flux

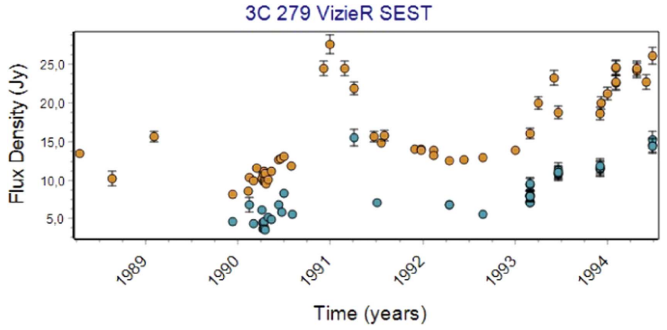


**Figure 1.** Flux densities of 3C 279 radio source observed with the SEST telescope at 90 and 230 GHz. Image adapted from the VizieR Catalog (Tornikoski et al. 1996).

state (Pian et al. 1999) allow the luminosity of the accretion disk to be estimated at $L_d \simeq 6.00 \times 10^{45}\,\mathrm{erg\,s^{-1}}$. The estimates of the mass of the central black hole are on the order of $3.00 \times 10^8\,M_\odot$, derived from the luminosity of broad optical emission lines (Woo & Urry 2002), $8.16 \times 10^8\,M_\odot$ of the width of the $H_\beta$ line (Gu et al. 2001) and $7.94 \pm 3.16 \times 10^8\,M_\odot$ of the luminosity of the host galaxy (Nilsson et al. 2009). The object possesses a compact, milliarcsecond-scale radio core and a jet with time-variable structure. Multi-epoch radio observations conducted between 1998 and 2001 (Jorstad et al. 2004, 2005) provided an estimate of the bulk Lorentz factor of the radio-emitting material, $\Gamma_j = 15.5 \pm 2.5$ and the direction of motion to the line of sight, $\theta_{\rm obs} = 2\overset{\circ}{.}1 \pm 1\overset{\circ}{.}1$, which corresponds to a Doppler factor of $24.1 \pm 6.5$. (Hayashida et al. 2015).

3C 279 presents variability of short and long periods (Aller et al. 2011; Rani et al. 2017). Rapid variability was also observed in the SEST monitoring project, where the sources have been observed during several years at 90 and 230 GHz (Tornikoski et al. 1996). The flux density at 90 GHz is higher than 230 GHz in a average ratio (higher/lower) of ≈250% and a strong correlation can be observed in these frequencies during this period as seen in Figure 1.

### *1.2. Properties of Blazar 4C +29.45*

The blazar 4C +29.45 (1156+295) ($z = 0.729$) is an archetypal radio-loud AGN with a prominent jet (Zhao et al. 2011). It is variable across the entire spectrum. Strong $\gamma$-ray outbursts have been detected by EGRET and *Fermi* at energies higher than 100 MeV (Thompson et al. 1995; Mukherjee et al. 1997; Hartman et al. 1999; Abdo et al. 2009). In the optical domain, the source has been classified as an OVV source and a highly polarized quasar (HPQ; Wills et al. 1983, 1992; Glassgold et al. 1983). In the radio domain, 1156+295 displays a significant variability on timescales from years to days (e.g., see MOJAVE monitoring program) and in two-year monitoring of intra-day variability (Liu et al. 2013). On a wide range of linear scales from paresecs to kiloparsecs, the source has a core-jet structure (Zhao et al. 2011). The jet is curved and consists of several bright knots. On parsec scales, the jet initially points to the north and then bends to the northeast at a distance of 3–4 mas from the core. At about 25 mas from the core, the jet then bends northwest and aligns itself with the initial direction of the kiloparsec-scale jet. On kiloparsec scales, the jet has a wiggling morphology around a mean position angle of about −18° and

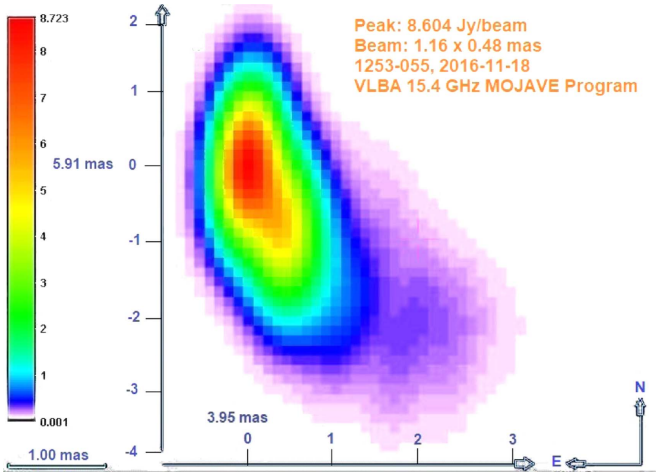


**Figure 2.** Recent map of object 3C 279 VLBI (1253-055) obtained from MOJAVE in 2016 November 18. The region of the core plus the components presents variability of peak for each map.

terminates at a hotspotthat is 2 arcsec north of the core (Hong et al. 2004). On the basis of the high apparent superluminal velocities (up to 15 $h^{-1}$ c), where $h$ is the Hubble constant in units of 100 $\mathrm{km\,s^{-1}\,Mpc^{-1}}$ (McHardy et al. 1990), VLBI jet components and ultra-high brightness temperatures ($>10^{12}$ K) of the core component (Piner & Kingham 1997; Jorstad et al. 2001; Hong et al. 2004), the angle between the jet axis and the line of sight is quite small. The complex bending jet can be attributed to the projected shape of a 3D helical jet (Hong et al. 2004), which appears to be common in radio-loud AGNs (Conway & Murphy 1993).

## 2. Observations and Data Reduction

The idea is to use the maps of the MOJAVE (VLBI) converted into light curves. Currently, the OVV Quasar 3C 279 presents 111 maps obtained from 1995 July 28 until 2016 November 18. The MOJAVE project has observations that are not equally spaced, but this fact should not be a restriction for this work, which aims to reconstruct the light curve modeled by equations that generate flux densities to fit these observations that present outbursts during a given period.

Figure 2 shows one from a series of images used in the conversion to the light curve.

The technique used consists in converting a set of images in light curves, obtaining the properties of core and the individual components, such as the position (R.A./decl.), the length of the semimajor axis and the eccentricity of each component observed in each map. Each VLBI image is obtained by its corresponding Fits file, which contains the beam size, the increment of each pixel in degrees (normally ≈$2.7778 \times 10^{-8}$ degrees), and the average noise (rms) that was considered. All these values are parameters of the equations to obtain the flux density as a function of the peaks from the observations in jansky/beam. With this, the flux density $F$ of the jet components can be estimated from a light curve converted from a VLBA map through

$$a_{\rm beam}^{\rm FWHM} = 2\sqrt{2\ln(2)}\,a_{\rm beam}, \qquad (1)$$

**Table 1**
Definition of the Parameters to be Calculated by the Method to Obtain the Fit of the Light Curve

| Parameter | Description | Units |
|---|---|---|
| $\Delta S_{(\max)}$ | Maximum amplitude of the outburst | Jy |
| $t_0$ | Initial date of the outburst | Date/Time |
| $\tau$ | Rise time | Days |
| $Q_f$ | Quiescent jet flux density | Jy |

where $a_{\text{beam}}^{\text{FWHM}}$ is the effective size of the optimized components and $a$ is the calculated size of the semimajor axis,

$$F_{(\text{comp})} = 8 \ln 2 \left( \frac{a^2 \sqrt{1-\epsilon^2}}{a_{\text{FWHM}}^{\text{beam}} b_{\text{FWHM}}^{\text{beam}}} \right) I_0, \quad (2)$$

where $b_{\text{FWHM}}^{\text{beam}}$ is the FWHM in units of pixels of the minor synthesized beam axes, $\epsilon$ is the elliptical eccentricity, $I_0$ is the central intensity in units of jansky/beam and $F$ in jansky is the flux density converted for each component for each date of the VLBA map (Caproni et al. 2011).

Figure 2 shows the beam area as (1.16 × 0.48) mas. The beam area may be different for each observation, so the total flux density is given by

$$F_{(\text{total})} = \sum_{i=1}^{n} F_{(\text{comp}_i)}, \quad (3)$$

where $n$ is the number of components for each MOJAVE object. In the case of 3C 279, a total of nine were considered, meaning the core plus eight components (Lister et al. 2009b) and VizieR Catalog Table 1 (Ochsenbein et al. 2000). Using these equations, the model reached levels of flux densities very closed to those obtained by the UMRAO Database. Then, the set of $F_{(\text{total})}$ obtained forms each point to the light curve on the respective date.

Figure 3 shows the source 3C 279 at 14.5 GHz.

The purpose of the use of this light curve is the comparison with the transformations of the VLBA maps to a similar curve from Michigan at the same period. The comparison with this curve, ensures that the MOJAVE data becomes similar to the UMRAO database. The Michigan light curve was also used to verify if all calculated parameters are in a range as expect. If the values found in the MOJAVE calculation fit to the UMRAO, even with a larger observation interval, it will be enough for an accurate result.

The conversion of all MOJAVE maps according to Equations (1)–(3) results in the following light curve, as shown in Figure 4.

The light curves above have a common period between 1996 and 2012, where we can see a similarity between the periods of evident peaks on May 1999 and May 2012, by comparison between UMRAO (14.5 GHz) and MOJAVE (15.3 GHz).

## 3. The Light-curve Approach

The approach of the model predicts that a parameterized analytic function can solve the variability of the curve in terms of more stable fluxes (or quiescent) and also when there are overlapping peaks. In our approach, there are four parameters.

The maximum amplitude of the outburst is the flux density difference between $t_0$ and $t_{\max}$. The parameters are free assuming that the CE can calculate these events as outbursts.

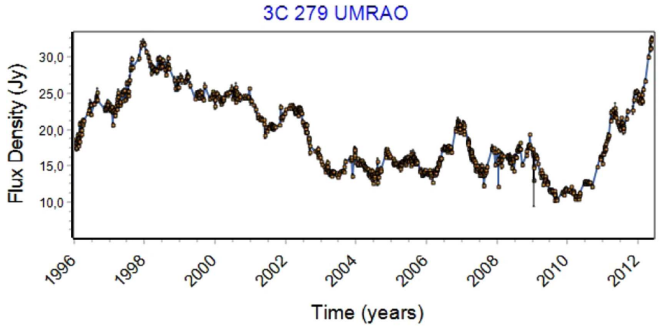


**Figure 3.** Light curve obtained from UMRAO database for 3C 279 at 14.5 GHz. (Contribution of the site of Michigan Astronomy, https://dept.astro.lsa.umich.edu).

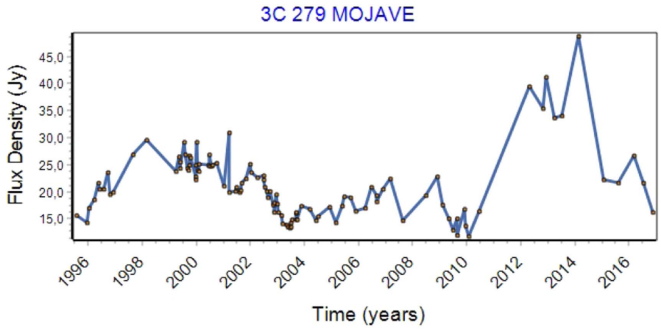


**Figure 4.** Light curve obtained from MOJAVE 3C 279, where we can see the plotted points originated by the conversion from 111 dates as seen in Equation (3).

### 3.1. Setting the Number of Outbursts

The imposition of the number of outbursts is not the most important property of the model, due the fact that the interval between observations may vary. We can establish that there is an approximate average of 70 days between observations for 3C 279 and approximately 133 days for 4C +29.45 in the MOJAVE; however, estimating some events incrementally is a key factor for the decomposition. Obviously, the more outbursts we can infer in the model, the better the results will be (Türler et al. 1999b). Rather than a precise number, we present in this article an evolution of results with additions (specifically from 24 to 33 events). A minimum number of outbursts is proposed in this work, simply by the fact that the overlapping observations of minor events, which can be fit with the observations at 15.3 GHz, is enough to get the main features of the shock-wave model on a macroscopic scale. Also it is not an aim of this work to determine the exact number of overlaps and its properties, but a possible scenario of the decomposition in lower scales. The parameters presented in the functions allow only a very limited number of overlaps for each number of outbursts. The sum of least squares of the flux density in each date is sufficient for the determination of the best parameters, usually applied to obtain the best fit.

### 3.2. Setting the Parameters for Shock Waves

As in the model presented by Hovatta et al. (2009), the flux density observed as a function of time $S(t)$ for a single outburst with an amplitude $\Delta S_{(\max)}$, starting at the time $t = t_0$ and peaking at $t = t_0 + t_{(\max)}$, where $t_0$ is the starting epoch of outburst and $t_{\max}$ is the epoch when the flux density reaches the

maximum in the light curve, is given by

$$\Delta S(t) = \Delta S_{(\max)} e^{(t-t_{\max})/\tau} \quad (4)$$

if $t_0 <= t_{\max}$ and

$$\Delta S(t) = \Delta S_{(\max)} e^{(t_{\max}-t)/1.3\tau} \quad (5)$$

if $t_0 > t_{\max}$.

The exponents $\tau$ define the rise time of the outburst. It may be observed by Equation (5) that the estimated time of decline is longer than the rise time in the ratio of 1.3 (Valtaoja et al. 1999). The parameters $\Delta S_{(\max)}$, $t_0$ and $\tau$ assume continuous values in functions, i.e., these values are not functions of $\nu$. An additional parameter $Q_f$ was also used to define the quiescent jet flux density value. Litchfield et al. (1995) found a value of $8.55 \pm 0.15$ to 22 GHz to 3C 279 and for 4C +29.45 there is a quiescient jet flux below 0.5 Jy at 43 GHz and 4.8 GHz (Liu et al. 2013). The CE method should find the best values for these parameters to fit the entire light curve.

The intervals allowed for the calculation are

$$8.50 \leqslant \Delta S_{(\max)} \leqslant 50.0 \text{ Jy for 3C 279},$$
$$0.1 \leqslant \Delta S_{(\max)} \leqslant 35.0 \text{ Jy for 4C + 29.45},$$

$t_0 \geqslant$ the lowest epoch of light curve and $t_0 \leqslant$ the highest epoch of the light curve

$$50.0 \leqslant \tau \leqslant 732.0 \text{ days for 3C 279},$$
$$40.0 \leqslant \tau \leqslant 732.0 \text{ days for 4C + 29.45},$$
$$5.0 \leqslant Q_f \leqslant 8.6 \text{ Jy for 3C 279 and}$$
$$0.1 \leqslant Q_f \leqslant 0.5 \text{ Jy for 4C + 29.45}.$$

The constrained values of these parameters do not restrict the results, the allowed ranges' limits are much smaller and much larger than the observations and would be free enough for the complete parameterization of the functions. It should be observed that despite being a free parameter, the first outburst $\Delta S_{(\max)}$ must be followed by the reason for determining the possibles dates of occurrence of the other outbursts, as the effect of phase adjustment of the functions. In fact, the first outburst encountered by the method will determine the possible cadence of shock waves. This work assumes that the observed peaks in a light curve are basically the result of the shock waves composed by quiescent flux density and outbursts.

### 3.3. Model Fitting

Model fitting is a technique that is generally used for solving the inverse problems in which the true distribution of a certain variable needs to be recovered from the measured distribution (Lobanov 1996). In this work, model fitting produces a parametric model by using Equations (4) and (5), where $\Delta S_{(\max)}$, $t_0$, $\tau$ and $Q_f$ are the variables, or also called parameters. These results are compared with the observed measurements, and the difference between the observation and the calculations is used for the adjustment of the model.

## 4. The Cross Entropy Method

The CE method was motivated by an adaptive algorithm for estimating probabilities of rare events in complex stochastic networks (Rubinstein 1997), which involves variance minimization. It was soon realized (Rubinstein 1999, 2001) that a simple CE modification of Rubinstein (1997) could be used not only for estimating probabilities of rare events but for solving difficult cost of production as well. This is done by converting the "deterministic" optimization problem into a related "stochastic" optimization problem and then using rare event simulation techniques similar to Rubinstein (1997). Several recent applications demonstrate the power of the CE method (Rubinstein 1999) as a generic and practical tool for solving NP-Hard problems. An NP-Hard problem means "at least as hard as any NP-Problem" (nondeterministic polynomial time; Weisstein 2005). The CE method involves an iterative procedure, where each iteration can be broken down into two phases.

The main algorithm of the CE for a Gaussian minimization can be described as follows: we define $\chi$ as a finite set of states and $S$ a function of performance calculated on $x$. We want to find the minimum value of $S$ in $\chi$, and the corresponding status when the minimum is obtained. So,

$$S(x^*) = y^* = \min S(x) \ \{x \in X\}, \quad (6)$$

where $y^*$ is the minimal value and $S(x^*)$ is a performance function.

The starting point of the CE methodology is to associate a estimation problem with an optimization problem (Equation (6)). To this goal, we have selected the best of solutions $I_{S(x)\leqslant y}$ from set $\chi$ and their indicators of a series of attempts. After we left $\{f(.;h), h \in H\}$ as a set of "Probability Density Function" (pdf) discrete in $\chi$, parameterized by the associated values of a vector $h$. For a given $u \in H$, we associate with Equation (6) the problem of minimizing $S(x)$ and estimating the number:

$$\ell(y) = P_u(S(X) \leqslant y) = \sum_x I_{(S(x)\leqslant y)} f(x, u) = E_u I_{(S(x)\leqslant y)} \quad (7)$$

(Kroese et al. 2006), where $P_u$ is the probability in which the random status $\chi$ has the pdf $f(.;u)$ and $E_u$ represents the corresponding operator. We call the estimation problem (Equation (7)) the associated stochastic problem (ASP). To indicate how the Equation (7) is associated with Equation (6), we assume, for example, that $y$ is equal to $y^*$ and $f(.;u)$ is the uniform density on $\chi$. We note that, typically, $\ell(y^*) = f(x^*; u) = 1/|X|$, where $|X|$ represents the number of elements in $X$, a very small number. So, for $y = y^*$, a natural way to estimate $\ell(y)$ would be the use of the estimator $LR$ (Kroese et al. 2006)

$$\hat{\ell}(y) = \frac{1}{N_1} \sum_{i=1}^{N_i} I_{(S(X_i)\leqslant y)} W(X_i; u; \hat{h}T) \quad (8)$$

$$W(x, u, w) = \frac{f(x,u)}{f(x,w)}. \quad (9)$$

Where $T$ represents the final number of iterations and $LR$ would have as reference the parameter $h^*$ given by

$$h^* = \arg_h \min E_u I_{(S(X_i)\leqslant y)} lnf(X; h). \quad (10)$$

This parameter could be estimated by

$$\hat{h}^* = \arg_h \min \frac{1}{N} \sum_{i=1}^{N} I_{(S(X_i)\leqslant y)} lnf(X_i; h), \quad (11)$$

where $\chi$ is generated by the (pdf) $f(.;u)$.

### 4.1. The Adaptation of the Cross Entropy Method for the Modeling of Light Curves

We can consider a light curve as a set of points of amplitudes $S(x)$. Assuming that $S(x)$ can be described by an analytical shock-wave model with $Np$ parameters $p1, p2, ..., pNp$, we can use the CE optimization method to search for the set of parameters $x^* = (p_1^*, p_2^*, ..., p_{N_p}^*)$, where the CE finds the best description of the amplitudes for the model (Rubinstein 1999; Kroese et al. 2006). The $S(x)$ is calculated as flux density in jansky. The optimization process is calculated by random generation for $N$ independent sets of parameters $X = (x_1, x_2, ..., x_N)$, where $x_i = (p1_i, p2_i, ..., pN_{pi})$, and minimizing an optimization (or performance) function $S(x)$ used to verify the quality of fit during the computational process. In an ideal situation, in which all the parameters have converged to an exact solution, we must obtain $S(x^*) \to 0$. To find the best solution of optimization of the CE, we start the process defining a range of parameters in which the algorithm searches the best candidates: $p_j^{\min} \leqslant p_j(t) \leqslant p_j^{\max}$, where $t$ represents the iteration number. By introducing $\bar{p}_j(0) = (p_j^{\min} + p_j^{\max})/2$ and $\sigma(0) = (p_j^{\max} - p_j^{\min})/2$, we can compute $X(0)$ from:

$$X_{ij}(0) = \bar{p}_j(0) + \sigma_j(0) M_{ij}, \tag{12}$$

where $M_{ij}$ is a light curve matrix with random values generated from a zero-mean normal distribution with a standard deviation of unity.

The next step is to calculate $S_i(0)$ for each set of $x_i(0)$, ordering by increasing values of $S_i$. Then the first $N_{\rm elite}$ set of parameters is selected, i.e., the $N_{\rm elite}$ sample with the lowest $S$-values, which will be referred to as the elite sample matrix $X^{\rm elite}(0)$.

Let $\underline{\iota}$ be the indices of the $N^{\rm elite}$ best performing (=elites) samples. Update for all $j = 1, ...., n$ let

$$\tilde{\mu}_{tj} = \sum_{i \epsilon \underline{\iota}} \frac{X_{ij}}{N^{\rm elite}} \tag{13}$$

and

$$\tilde{\sigma}_{tj}^2 = \sum_{i \epsilon \underline{\iota}} \frac{(X_{ij} - \mu_{tj})^2}{N^{\rm elite}}, \tag{14}$$

where $\tilde{\mu}$ and $\tilde{\sigma}$ are the mean and the standard deviation respectivately. (Kroese et al. 2006).

Smooth

$$\hat{\mu}_t = \alpha \tilde{\mu}_t + (1 - \alpha) \hat{\mu}_{t-1} \tag{15}$$

and

$$\hat{\sigma}_t = \alpha \tilde{\sigma}_t + (1 - \alpha) \hat{\sigma}_{t-1}. \tag{16}$$

The reason for using the dynamic smoothing for $\sigma$ instead of a fixed smoothing can be explained as follows. With a fixed $\alpha$, the convergence to a degenerate distribution will typically happen too quickly, which will in turn result into a sub-optimal solution (also called a local solution). The goal of Equations (15) and (16) is precisely to prevent this. It is readily seen that by choosing for $\sigma$ the value smoothed updating instead of the $\alpha$ one, the convergence to the degenerate case will have a polynomial speed instead of exponential (Kroese et al. 2006).

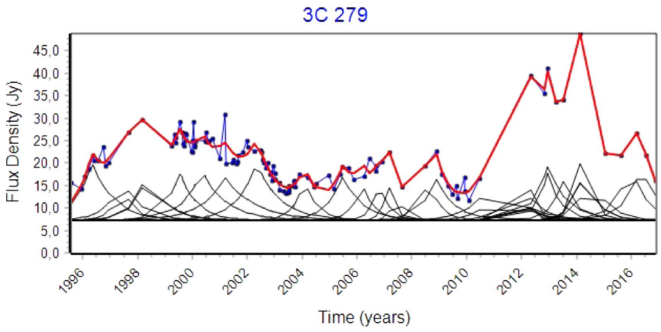


**Figure 5.** CE method calculated the best fit for ≈33 outbursts for 3C 279, where at the end of the iterations the best distribution of shock waves was found. The straight line with the minimum value represents the best estimated value of the quiescent flux density.

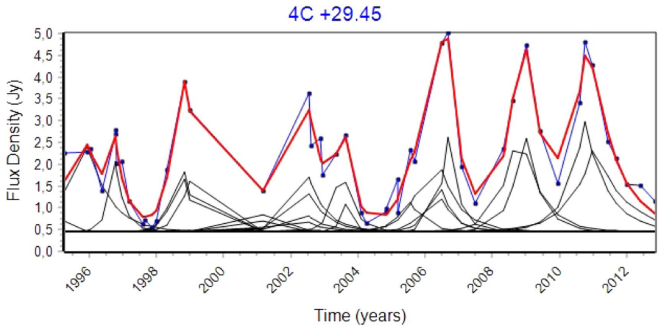


**Figure 6.** CE method calculated the best fit for ≈24 outbursts for 4C +29.45.

The matrix $X$ at the next iteration is computed as

$$X_{ij}(1) = \bar{p}_j^{\rm elite}(0) + \sigma_j^{\rm elite}(0) M_{ij}. \tag{17}$$

The algorithm continues to be processed by function (7) for $M_{ij}$ recalculated for each iteration. The optimization calculation ends when the maximum number of iterations $t_{\max}$ is reached or the sum of the $\sigma$ is less than $1.0 \times 10^{-10}$. This tolerance value is a very small number and has no effect on the results.

### 4.2. Defining the Performance (or Objective) Function

Let us consider the optimization function $S$ calculated by $S_m(t)$ at a given flux density $m$ and iteration $t$ defined as the squared difference between the observed flux $F_m$ and the generated model flux $M_m(t)$, so $S_m(t) = [F_m - M_m(t)]^2$. The sum of the residual value of the model fitting $R(t)$ can be calculated from

$$R = \sum_{m=1}^{N_{\rm date}} R_m(t), \tag{18}$$

where $N_{\rm date}$ is the number of observed dates (points in the light curve). The lowest value for $R$ means a best calculated performance, as a method of the sum of least squares.

## 5. Results

Figures 5 and 6 show the results by the decomposition of about 33 outbursts for 3C 279 and ≈24 outbursts for 4C +29.45 respectively. The main properties of the light curve are observed.

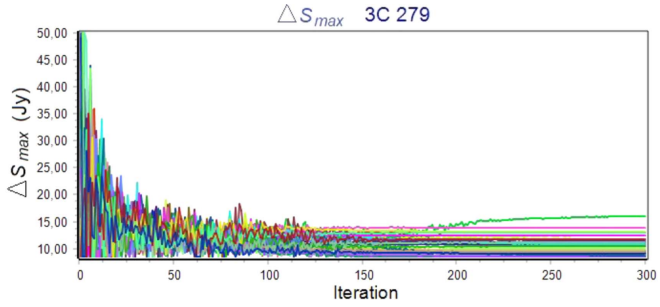


**Figure 7.** Convergence of $\Delta S_{\max}$ values for each estimated outburst.

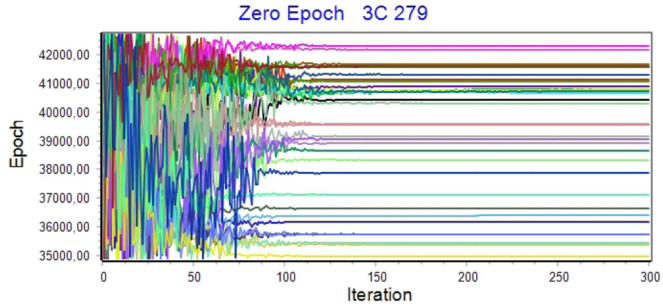


**Figure 8.** Convergence of Times (Zero Epoch) found for each outburst of 3C 279.

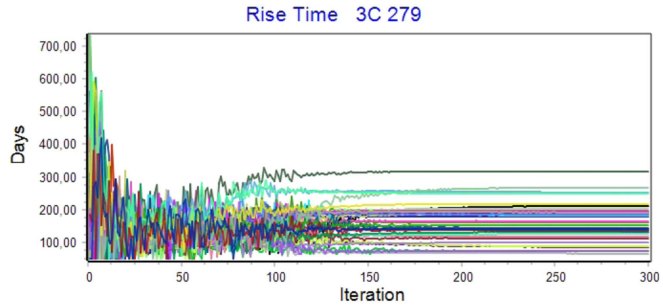


**Figure 9.** Values obtained from the rise time for each outburst of 3C 279. The limits were determined from about 50.0 to 732.0 days. No rise time was found below 66 or above 318 days.

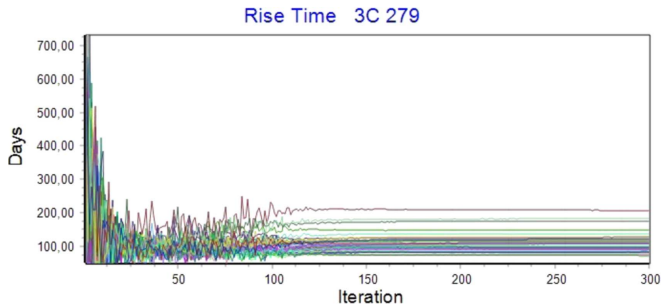


**Figure 10.** Values obtained from the rise time for each outburst of 3C 279 calculated from the Michigan Database.

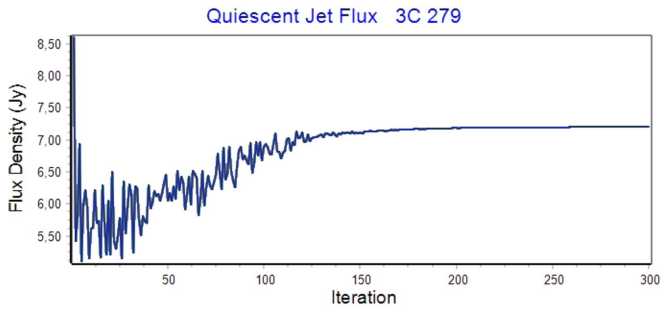


**Figure 11.** Calculation of convergence for the quiescent jet flux density.

Figure 5 shows the fitting found for decomposition into smaller components based on self-similar formations at 15.3 GHz.

The flux density converted by Equations (1), (2), and (3) had a good fit for 3C 279 and 4C +29.45. In Figure 7, the $\Delta S_{\max}$ for each outburst are shown. Even with free parameters, one can see a convergence to an estimated average value.

The limits were fixed from 8.5 to a maximum of 50.0 Jy. The CE found values between ≈8.5 and ≈16.02 Jy for individual outburst. Each line represents the evolution in the search for better results, in this case, for $\Delta S_{\max}$ of each shock wave. CE starts by varying values until it finds a better and more stable value. A stable value means that the sigma value of each parameter for each outburst has automatically decreased enough to obtain the best values, indicated in Figure 7 when the variations end.

In Figure 8, the initial epochs of each outburst are shown as one of the parameters.

CE starts calculating the parameter $t_0$ until the best set of dates is found. The variations of values at the beginning of the calculation are wide because the value of $\sigma$ is large. So $\sigma$ becomes smaller in each iteration, according to Equation (14).

Figure 9 shows the interval found for the smallest and largest rise times for 3C 279 (MOJAVE), as a dispersion. The figure shows the predominance of values within a range.

Figure 10 shows the interval found for the smallest and largest rise times for 3C 279, calculated from the UMRAO Database.

The parameters are the same as those used in the converted light curve of the MOJAVE. No period was found below 70 or above 182 days, including the fact that the rise times over ≈120 days are dominant. The calculation made with the light curve of the UMRAO is a way of showing that there is a strong similarity between the results found in the converted curve light curve of the MOJAVE VLBI, which guarantees, for example, the use of the rise time in the calculation of the brightness temperature. Figure 11 shows the variation during the search for the best value for the quiescent jet flux density for 3C 279.

The convergence of variations of $S_{\max}$, $t_0$, $\tau$, and $Q_f$ to stable values means that the equations of the shock-wave model fit the observations (or represent the physical reality of the AGN), because the $\sigma$ value for each parameter becomes smaller at each iteration due to the entropy decrease. Due to the fact that the 100 parameters, $(3 \times 33) + 1$ for the quiescent jet flux density, are calculated at the same time at each iteration, there is a strong dependence between them. So, a unique and best value for the quiescent jet flux density is obtained to fit the entire light curve according to the calculation of all other parameters.

Table 2 shows the cross-reference according to Figures 7, 8, 9, and 11, for the best parameters.

Table 3 shows the cross-reference for the best 73 parameters $(3 \times 24 + 1)$ for 4C +29.45.

### *5.1. Obtaining the Speed of the Components and the Apparent Superluminal Motion*

Superluminal motion is the "faster-than-light" motion seen in some radio galaxies, BL Lac objects, and quasars. All of

**Table 2**
The Best Values Found for Each Parameter of the 33 Outbursts for 3C 279

| Seq. | $\Delta S_{max}$ (Jy) | $t_0$ Zero Epoch | $\tau$ (days) |
|---|---|---|---|
| 2 | 9.731 | 1996 Nov 13 | 191 |
| 1 | 13.118 | 1995 Sep 26 | 218 |
| 3 | 8.501 | 1997 Jan 14 | 125 |
| 4 | 11.648 | 1997 Nov 11 | 186 |
| 5 | 11.245 | 1997 Nov 21 | 187 |
| 6 | 10.824 | 1999 Jan 17 | 179 |
| 7 | 11.176 | 1999 Aug 23 | 253 |
| 8 | 9.547 | 2000 Apr 27 | 318 |
| 9 | 12.891 | 2001 Aug 23 | 248 |
| 10 | 9.079 | 2003 Sep 06 | 140 |
| 11 | 10.093 | 2004 Dec 02 | 203 |
| 12 | 8.500 | 2005 Oct 21 | 132 |
| 13 | 8.731 | 2006 Jul 07 | 100 |
| 14 | 8.501 | 2006 Dec 03 | 73 |
| 15 | 8.504 | 2007 Mar 24 | 66 |
| 16 | 9.811 | 2008 Apr 11 | 116 |
| 17 | 9.432 | 2008 May 11 | 191 |
| 18 | 11.126 | 2010 Apr 27 | 268 |
| 19 | 9.181 | 2010 Aug 30 | 211 |
| 20 | 10.810 | 2011 May 04 | 181 |
| 21 | 8.743 | 2011 Jun 11 | 133 |
| 22 | 12.441 | 2011 Aug 17 | 88 |
| 23 | 16.017 | 2011 Aug 24 | 74 |
| 24 | 11.381 | 2011 Dec 08 | 86 |
| 25 | 12.387 | 2012 Jun 05 | 194 |
| 26 | 10.537 | 2012 Jul 24 | 139 |
| 27 | 9.410 | 2013 Jan 29 | 144 |
| 28 | 10.398 | 2013 Oct 20 | 153 |
| 29 | 12.919 | 2013 Oct 20 | 113 |
| 30 | 11.681 | 2013 Nov 13 | 138 |
| 31 | 11.748 | 2014 Jan 22 | 161 |
| 32 | 13.813 | 2015 Jun 15 | 166 |
| 33 | 12.362 | 2015 Oct 17 | 197 |

**Note.** The quiescent jet flux density optimized for this set of parameters is ≈7.02 Jy, according to Figure 11.

**Table 3**
The Best Values Found for Each Parameter of the 24 Outbursts for 4C +29.45

| Seq. | $\Delta S_{max}$ (Jy) | $t_0$ Zero Epoch | $\tau$ (days) |
|---|---|---|---|
| 1 | 2.482 | 1995 Apr 07 | 192 |
| 2 | 0.669 | 1995 Apr 07 | 40 |
| 3 | 1.607 | 1996 Jul 21 | 81 |
| 4 | 2.105 | 1998 May 31 | 99 |
| 5 | 1.838 | 1998 Jun 02 | 98 |
| 6 | 1.260 | 1998 Aug 29 | 112 |
| 7 | 0.211 | 1999 Jun 15 | 130 |
| 8 | 0.392 | 2000 Sep 17 | 161 |
| 9 | 0.256 | 2000 Oct 20 | 132 |
| 10 | 0.665 | 2001 Jul 20 | 147 |
| 11 | 0.541 | 2001 Oct 28 | 171 |
| 12 | 1.095 | 2001 Dec 20 | 162 |
| 13 | 1.481 | 2002 Jan 11 | 152 |
| 14 | 1.690 | 2003 Mar 23 | 99 |
| 15 | 0.692 | 2003 Jun 18 | 58 |
| 16 | 0.815 | 2005 Feb 12 | 129 |
| 17 | 2.422 | 2005 Sep 21 | 167 |
| 18 | 1.378 | 2005 Nov 22 | 124 |
| 19 | 1.425 | 2006 Jan 17 | 109 |
| 20 | 2.191 | 2006 Jun 02 | 94 |
| 21 | 2.659 | 2008 Apr 17 | 173 |
| 22 | 2.635 | 2008 Jul 27 | 130 |
| 23 | 2.539 | 2010 Mar 17 | 196 |
| 24 | 1.969 | 2010 Apr 22 | 261 |

**Note.** The quiescent jet flux density optimized for this set of parameters is ≈0.45 Jy.

these sources are thought to contain a black hole, responsible for the ejection of mass at high velocities, as seen in Figure 12.

At the first observation, the peak component is at a distance $|\boldsymbol{R}|$ from the observer and moving at an angle $\theta$ to the line of sight, where $\theta = 0°$ is the motion completely along the line of sight, and $\theta = 90°$ is the motion completely perpendicular to the line of sight. A second observation is taken after an elapsed time, $\Delta t$, has passed. In this amount of time, the component has moved $v\Delta$t along its path. From geometry, this means that the component is now $v\Delta t \cos\theta = |\boldsymbol{r}|\cos\theta$ closer to the observer than at the first observation. Thus it will take a time $t_1 = \frac{|\boldsymbol{R}|}{c}$ for the light from the component to reach the observer for the first observation, and a time $t_2 = \frac{(|\boldsymbol{R}| - v\Delta t\cos\theta)}{c} + \Delta t$ for the light from the component to reach the observer for the second observation. Meanwhile, in the time $t_2$–$t_1$, the component has moved across the sky a distance of $rvt = v\Delta t \sin\theta$, from the point of view of the observer. Therefore, the observer sees an apparent motion across the sky of

$$v_{app} = \frac{|\boldsymbol{R}|}{t_2 - t_1}. \quad (19)$$

The descrition of Equation (19) is standard in AGN/VLBI science, a complete reference can be found in Zensus & Pearson (1987).

We obtained the velocity of the components directly from the MOJAVE website, where we can see from the table a maximum speed of 3C 279 of 651 ± 25 $\mu$as yr$^{-1}$ (20.58 ± 0.79 c) for (C7) and a mean speed of 348 ± 2.2 $\mu$as yr$^{-1}$ (11.013 ± 0.069 c) for all components (Lister et al. 2013), as shown in Figure 13.

Bloom et al. (2013) found that the data for each of these components are consistent with significant changes to Lorentz factor, viewing angle and azimuthal angle, suggesting jet bending with changes in speed and observed Lorentz factors in the range of $\Gamma = 10 - 41$, viewing angles in the range of $\theta = 0.^{\circ}1$–$5.^{\circ}0$, and intrinsic (source frame) flux density in the range $F_{\nu,\mathrm{int}} = 1.5 \times 10^{-9} - 1.5 \times 10^{-5}$ Jy. Considering the individual components, the Lorentz factor varies from $\Gamma = 11 - 16$ for $C1$, $\Gamma = 31 - 41$ for $C5$, $\Gamma = 29 - 41$ for $C6$, and $\Gamma = 9 - 12$ for $C8$. These ranges indicate that we cannot be looking at a single underlying jet flow speed, but may be seeing separate pattern speeds from shocks moving through the jet, or a combination of flow speed and pattern speed.

For 4C +29.45, we can see a maximum speed of 603 ± 48 $\mu$as yr$^{-1}$ (24.6 ± 1.9 c) for (C7) and a mean speed of 387.6 $\mu$as yr$^{-1}$ (15.8 c) for all components (Lister et al. 2013), as shown in Figure 14.

The direction of the jet is upward and to the left relative to the view angle. The speed obtained for C2 is 43.3 ± 6.6 $\mu$as yr$^{-1}$, with almost no proper motion, and it is always located at a distance of 4 mas from the core. Figure source: Mojave Monitoring Program Data Archive. Separation versus Time Plot for 4C +29.45.

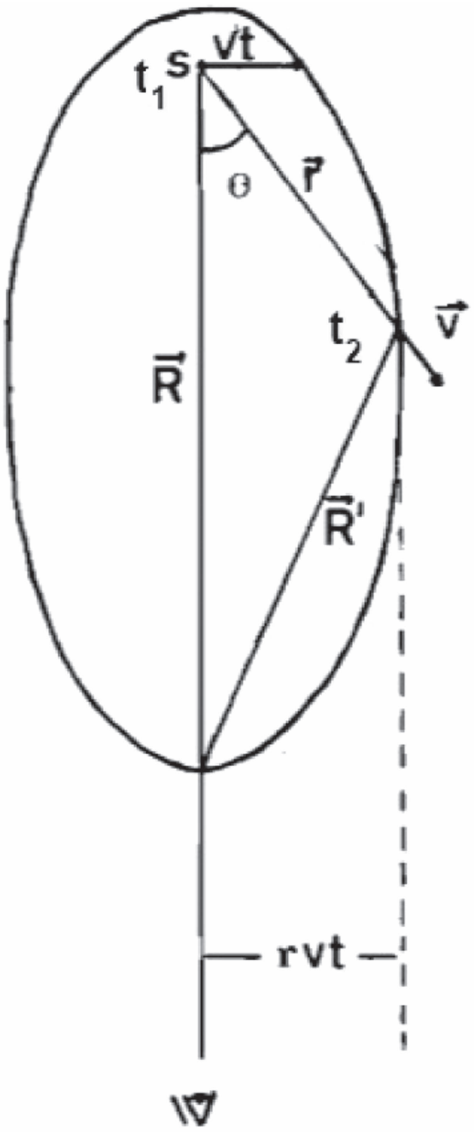


**Figure 12.** Schematic representation of a relativistic expansion for a speed $v$ seen by an observer. If $v \ll c$, this surface is a sphere of radius $vt$. If $v \sim c$, the distance that a particle with velocity $v$ seems to have moved at a time $t$, depends on its direction of motion, the Doppler factor $D$, and the Lorentz factor $\Gamma$ (Botti 1990).

### 5.2. The Doppler Factors, Lorentz Factors, and Viewing Angles

A way to calculate the factor Doppler using VLBI (Hovatta et al. 2009) is by flux density estimated and obtained by decomposition in exponential outbursts by calculating the timescale of variability of each outburst. With the calculation of $\Delta S_{\max}$ and the rise times of $\tau_{\rm obs}$, the temperature can be estimated as $T_{\rm obs} \propto T_{\rm int}$, where $T_{\rm obs}$ is the calculated temperature and $T_{\rm int}$ is the intrinsic temperature. Assuming that the time variability of intrinsic scale corresponds to the travel time of light. The Lorentz factor and the angle of sight can also be estimated by this correlation. The timescale obtained can be related by an intrinsic temperature on the order of $T_{\rm int} = 5.0 \times 10^{10}$ K (Lähteenmäki & Valtaoja 1999). Through the fitting calculated in Figure 5, we obtained the necessary parameters to estimate the brightness temperature of the

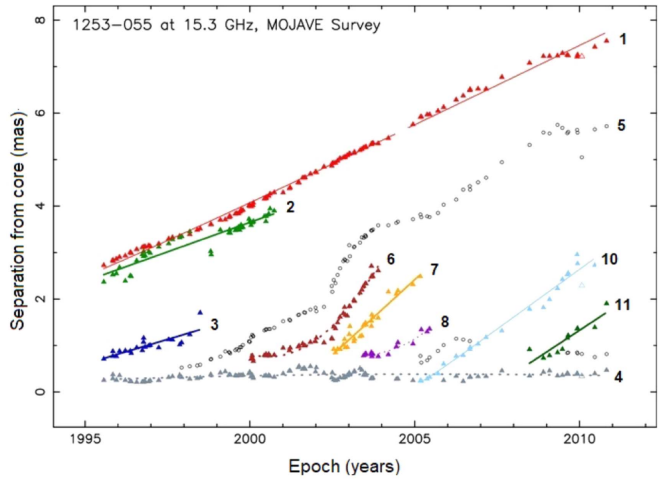


**Figure 13.** All the 3C 279 components' movements from VLBA images. The red line shows the trend speed for the movements obtained from C1 and a yellow line from C7. Figure source: Mojave Monitoring Program Data Archive. Separation vs. Time Plot for 3C 279.

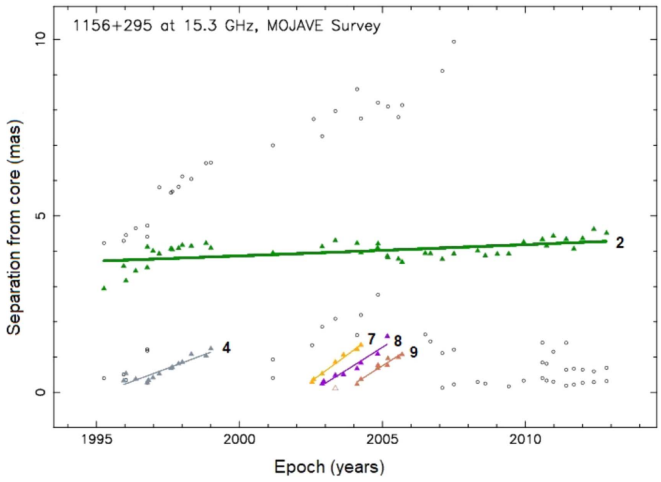


**Figure 14.** All the 4C +29.45 components' movements from VLBA images. The green line shows the trend speed for the movements obtained from C2 and a yellow line from C7.

sources 3C 279 and 4C+ 29.45:

$$T_{b,\rm var} = 1.548 \times 10^{-32} \frac{\Delta S_{\max} d_L^2}{\nu^2 \tau^2 (1+z)}, \quad (20)$$

where $\nu$ is the observed frequency in GHz, $z$ is the redshift, $d_L$ is luminosity distance in meters, and $\Delta S_{\max}$ and $\tau$ are defined by Equations (4) and (5), where $\Delta S_{\max}$ is the maximum amplitude (or flux density) in jansky, and $t_{\max}$ is the epoch of the flare maximum (Valtaoja et al. 1999). The standard $H_0 = 72$ km s$^{-1}$ Mpc$^{-1}$, $\Omega_m = 0.27$, and $\Omega_\Lambda = 0.73$ were used for this calculation for a uniform spherical source. The Doppler factor can be calculated by

$$D_{\rm var} = \left[\frac{T_{b,\rm var}}{T_{b,\rm int}}\right]^{1/3}, \quad (21)$$

where the suggested temperature is $T_{b,\rm int} = 5.0 \times 10^{10}$ K (Readhead 1994).

Comparing the Doppler factor with the apparent superluminal speed (or apparent transverse speed) $\beta_{\rm app}$, obtained by MOJAVE VLBI AGN samples, one can calculate the Lorentz

**Table 4**
Values Found by the CE Method for Log($T_b$), $D_{\rm var}$, $\Gamma_{\rm var}$, and $\theta_{\rm var}$ Obtained by $\Delta S$ and $\tau$ Minimum and Maximum Depending on the Variation Found by Parameters of Each Outburst

| Name | Ref. | $\nu$ | $z$ | Log($T_b$) | $D_{\rm var}$ | $\beta_{\rm app}$ | $\Gamma_{\rm var}$ | $\theta_{\rm var}$ |
|---|---|---|---|---|---|---|---|---|
| **3C 279** | **Min.** | **15** | **0.536** | **14.82** | **23.71** | **20.64** | **20.86** | **2.39** |
| **4C +29.45** | **Min.** | **15** | **0.729** | **14.43** | **17.59** | **24.85** | **26.38** | **3.07** |
| 3C 279 | Max. | 15 | 0.536 | 13.51 | 8.66 | 20.64 | 28.99 | 4.72 |
| 4C +29.45 | Max. | 15 | 0.729 | 13.27 | 7.22 | 24.85 | 46.47 | 4.25 |
| 3C 279 | Prev. | 15 | 0.536 | 14.84 | 24.00 | 20.64 | 20.90 | 2.40 |
| 4C +29.45 | Prev. | 15 | 0.729 | 15.06 | 28.50 | 24.85 | 25.10 | 2.00 |

**Note.** The values of the two first lines marked in bold refer to the best physical parameters found for comparison.

factor variability $\Gamma$ and the viewing angles $\theta$ using the Equations (22), (23), and (24), respectively:

$$\beta_{\rm app} = \frac{vt}{c} \tag{22}$$

$$\Gamma_{\rm var} = \frac{\beta_{\rm app}^2 + D_{\rm var}^2 + 1}{2D_{\rm var}} \tag{23}$$

and

$$\theta_{\rm var} = \arctan \frac{2\beta_{\rm app}}{\beta_{\rm app}^2 + D_{\rm var}^2 - 1}. \tag{24}$$

Table 4 shows the results obtained by CE using $\beta_{\rm app}$ from the speed of the components obtained from the MOJAVE project, both objects are type HPQ (High Polarization Quasar). The Ref. column indicates the use of the comparison between the minimum and maximum values found by the CE method depending on the variation found by parameters of each outburst.

The table also shows the results from (Prev.) analyses for comparison. The values of the two first lines marked in bold refer to the best physical parameters found for comparison. The "Max." values were discarded for this work.

The line referenced by "Prev." was obtained from Hovatta et al. (2009), where we note the comparison of the results for 3C 279 and 4C +29.45. By comparing the tables, we can see close values found for 3C 279, where the minimum values for rise time is applied. Some small differences were found in the Doppler factor, Lorentz factor, and viewing angle. For $D_{\rm var,}$ we can see the value of 24.0 in the previous analysis and 23.71 in the CE decomposition. This variation occurs due to the fact that the shortest rise time is on the order of ≈66 days, which leads to a small variation of brightness temperature and the log($T_{\rm obs}$) is very sensitive for the rise time. The differences found for 4C +29.45 to the Doppler factor and Lorentz factor are due to the fact that there is a large difference between the brightness temperature found in the CE calculation and the previous work. Even with free parameters, it would be necessary for CE to find, by example, an outburst with rise time on the order of 20 days and $\Delta S_{\rm max} \approx 0.66$ Jy or 34 days and $\Delta S_{\rm max} \approx 1.96$ Jy to reach the log($T_b$) ≈ 15.06, which was not possible during several calculations in this work, according to the results shown in Table 3.

## 6. Discussion

As shown above, it is possible to estimate with good accuracy the variabilities of the parameters $\Delta S$, $t_{0,}$ and $\tau$. The number of outbursts proposed in this article is a way to obtain an average for these parameters where the dispersion method of the values is applied, as shown in Table 4. Obviously, to estimate a precise value for this number would be ideal, but during testing we realized that the increase or decrease of the number of outbursts, at least from 24 to 33, generates a very similar variation in the dispersion of the results of the parameters. We consider this to be an acceptable inaccuracy due to the fact that the MOJAVE maps have not equally time spaced observations and the results remain close to that found in the article of Hovatta et al. (2009). Only larger variations become more evident when the number of outbursts is decreased from 16 to 12, where the rise time increases its mean values for ≈330 days, but with a very poor fitting. Another factor that could improve the results would be to fill the unknown points of the MOJAVE maps. Some points are spaced out for months, raising doubt to the possible values assumed in these intervals (gaps). A possible way to estimate component motions or even flux densities to obtain complementary data, such as interpolated data, is shown in Lobanov (1996), where the use of a model calculated by an algorithm can accurately detect unknown values in the combined study of kinematical and spectral evolution for quasar 3C 345. In that work, a polynomial fit can be seen in the two-dimensional trajectories, as a possible and likely reconstruction for the component's motion.

## 7. Conclusions

The decomposition of curves by a statistical method such as CE can be a useful tool to estimate both the amplitudes (flux density) as the rise time of the outbursts. The results obtained in this article show values close to those described in previous articles (Lindfors et al. 2006), where the variations of rise times are between 0.30 and 3.57 years at 43 GHz.

The equations to obtain the Doppler and Lorentz factors are sensitive to log($T_b$), which have imposed enough iterations to CE to get a rise time. An important factor that was detected during the adjustment of the curves by the CE is the fact that the formation of the first outbursts imposes a very important constraint on the entire curve, so, the number of possible scenarios for the decomposition becomes too small. In future work, we plan to apply this same technique to other frequencies to check the dispersions of the parameters in functions of $\nu$, i.e., suggesting links to $S(\nu)$ and $\tau(\nu)$ (Türler et al. 1999a).

The brightness temperatures found in this work, at least for 3C 279, depending on the rise time, are in agreement with previous works (Hovatta et al. 2009). In this work, for example, we used a minimum for $\tau \approx 66$ days for 3C 279, and the values found show predominant results for $\tau$ in the range of 95–190 days, as shown in Figure 9.

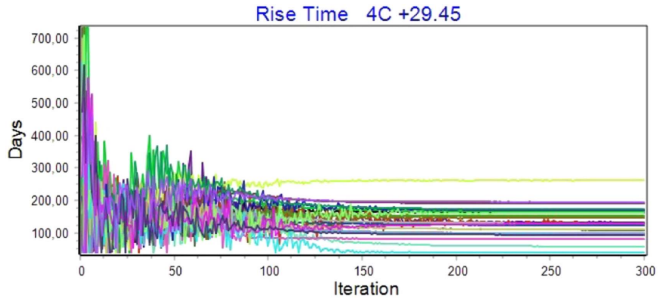


**Figure 15.** Convergence of the parameter $\tau$ when free values in the range of 40 to 732 days are applied.

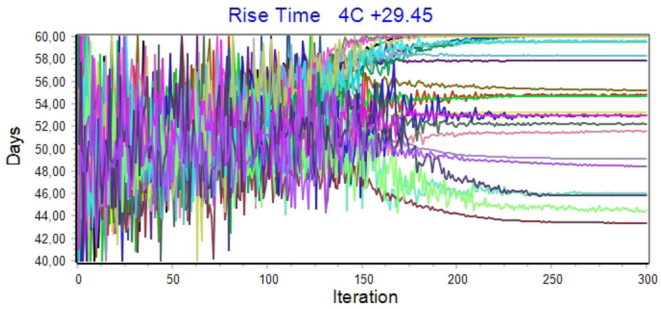


**Figure 16.** Convergence of values when the 60 day limit is an imposition to the CE for 4C +29.45. CE tries to find the best solution for $\tau$ over 60 days.

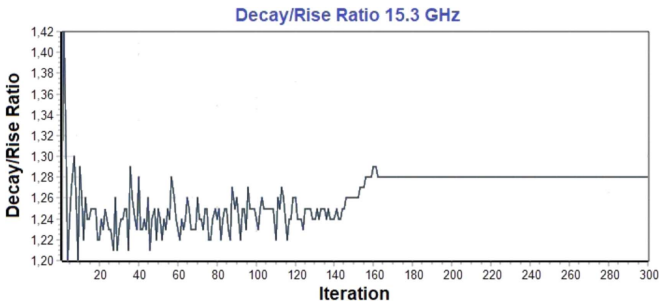


**Figure 17.** Convergence of the value for a free decay/rise ratio.

For 4C +29.45, a minimum of ≈40 days was found for $\tau$, and for this parameter the results are predominant in the range of 100–230 days, suggesting a lower brightness temperature, as shown in Figure 15.

To prove this fact, we impose during preliminary calculations a maximum of 60 days to $\tau$, and what happened was a CE searching for larger solutions, as shown in Figure 16.

While the $\tau$ varies from outburst to outburst, the spread is small and a unique typical decay/rise ratio could be used in Equations (4) and (5) for the entire light curve, as shown in Figure 17.

We found that there is a small variation in the decay/rise timescale ratio for 15.3 GHz. CE tends to estimate the best values (stable) in the range of 1.25–1.28; also, a good model fit is obtained using a $1.3\tau$ (Valtaoja et al. 1999), in which it was used in this work for comparison purposes.

In this work, we presented a method to estimate physical parameters such as the Doppler factor and the Lorentz factor through a method of statistical minimization. A way to ensure reliability in the results was to establish free parameters for the calculation, obviously within ranges whose results show physical values that make sense to the reality. Even with free parameters, it was possible to establish a relatively small dispersion for $\Delta S_{\max}$, $\tau$, and $Q_f$ as shown in Figures 7, 9, and 11, and we believe that this approach can represent the physical reality of these astrophysical objects.

This research has made use of data from the MOJAVE database, which is maintained by the MOJAVE team (Lister et al. 2009a).

This research has made use of data from the University of Michigan Radio Astronomy Observatory, which has been supported by the University of Michigan and by a series of grants from the National Science Foundation, most recently AST-0607523. Inclusion of the recent data in tables obtained as part of the *Fermi* program should include an acknowledgment to NASA *Fermi* grants NNX09AU16G, NNX10AP16G, and NNX11AO13G.

This research has made use of the VizieR catalog access tools, CDS, Strasbourg, France. The original description of the VizieR service was published by Ochsenbein et al. (2000).

Special thanks to Mrs. Margo Aller, from the Department of Astronomy (University of Michigan), for providing the 3C 279 light curve, which has been very important material for the development of this project.

Thanks go to ApJ's referee, editor, and staff for the detailed suggestions that helped this work become a proper article.

## ORCID iDs

R. P. Vitoriano https://orcid.org/0000-0002-9254-8190
L. C. L. Botti https://orcid.org/0000-0003-1424-0796

## References

Abdo, A. A., Ackermann, M., Ajello, M., et al. 2009, ApJ, 183, 46
Aller, M. F., Aller, H. D., & Hughes, P. A. 2011, JApA, 32, 5
Bloom, S. D., Fromm, C. M., & Ros, E. 2013, AJ, 145, 12
Botti, L. C. L. 1990, PhD thesis, National Institute for Space Research, INPE-5218-TDL/432
Caproni, A., Monteiro, H., Abraham, Z., Teixeira, D. M., & Toffoli, R. T. 2011, ApJ, 736, 68
Conway, J. E., & Murphy, D. E. 1993, ApJ, 411, 89
Glassgold, A. E., Bregman, J. N., Huggins, P. J., et al. 1983, ApJ, 274, 101
Gu, M., Cao, X., & Jiang, D. R. 2001, MNRAS, 327, 1111
Hartman, R. C., Bertsch, D., Fichtel, C. E., et al. 1992, ApJL, 385, L1
Hartman, R. C., Bertsch, D. L., Bloom, S. D., et al. 1999, ApJS, 123, 79
Hayashida, M., Nalewajko, K., Madejski, G. M., & Sikora, M. 2015, ApJ, 807, 79
Hong, X. Y., Jiang, D. R., Gurvits, L. I., et al. 2004, A&A, 417, 887
Hovatta, T., Valtaoja, E., Tornikoski, M., & Lähteenmäki, A. 2009, A&A, 494, 527
Jorstad, S. G., Marscher, A. P., Lister, M. L., et al. 2004, AJ, 127, 3115
Jorstad, S. G., Marscher, A. P., Lister, M. L., et al. 2005, AJ, 130, 1418
Jorstad, S. G., Marscher, A. P., Mattox, J. R., et al. 2001, ApJs, 134, 181
Kroese, D. P., Porotsky, S., & Rubinstein, R. Y. 2006, Methodol. Comput. Appl. Probab., 8, 383
Lähteenmäki, A., & Valtaoja, E. 1999, ApJ, 521, 493
Lindfors, E. J., Türler, M., Valtaoja, E., et al. 2006, A&A, 456, 895
Liodakis, I., Pavlidou, V., Hovatta, T., et al. 2017, MNRAS, 467, 4565
Lister, M. L., Aller, H. D., Aller, M. F., et al. 2009a, AJ, 137, 3718
Lister, M. L., Aller, M. F., Aller, H. D., et al. 2013, AJ, 146, 120
Lister, M. L., Cohen, M. H., Homan, D. C., et al. 2009b, AJ, 138, 1874
Litchfield, S. J., Stevens, J. A., Robson, E. I., & Gear, W. K. 1995, MNRAS, 274, 221
Liu, B.-R., Liu, X., Marchili, N., et al. A&A, 555, A134
Lobanov, A. P. 1996, PhD thesis, New Mexico Institute of Mining and Technology
Lynds, C. R., Stockton, A. N., & Livingston, W. C. 1965, ApJ, 142, 1667
Marscher, A. P., & Gear, W. K. 1985, ApJ, 298, 114
McHardy, I. M., Marscher, A. P., Gear, W. K., et al. 1990, MNRAS, 246, 305
Mukherjee, R., Bertsch, D. L., Bloom, S. D., et al. 1997, ApJ, 490, 116

Nilsson, K., Pursimo, T., Villforth, C., Lindfors, E., & Takalo, L. O. 2009, A&A, 505, 601
Ochsenbein, F., Bauer, P., & Marcout, J. 2000, A&AS, 143, 23
Pian, E., Urry, C. M., Maraschi, L., et al. 1999, ApJ, 521, 112
Piner, B. G., & Kingham, K. 1997, ApJL, 485, L61
Rani, B., Krichbaum, T. P., Lee, S.-S., et al. 2017, MNRAS, 464, 418
Readhead, A. C. S. 1994, ApJ, 426, 51
Richards, J. L., Max-Moerbeck, W., Pavlidou, V., et al. 2011, ApJS, 194, 29
Rubinstein, R. Y. 1997, Euro. J. Oper. Res., 99, 89
Rubinstein, R. Y. 1999, Methodol. Comput. Appl. Probab., 2, 127
Rubinstein, R. Y. 2001, in Stochastic Optimization: Algorithms and Applications, ed. S. Uryasev & P. M. Pardalos (Dordrecht: Kluwer), 303
Thompson, D. J., Bertsch, D. L., Dingus, B. L., et al. 1995, ApJS, 101, 259
Tornikoski, M., Valtaoja, E., Terasranta, H., et al. 1996, A&AS, 116, 157T
Türler, M., Courvosier, T. J. L., & Paltani, S. 1999a, A&A, 349, 45
Türler, M., Courvosier, T. J. L., & Paltani, S. 1999b, in ASP Conf. Ser. 159, BL Lac Phenomenon, ed. L. O. Takalo & A. Sillanpää (San Francisco, CA: ASP), 297
Valtaoja, E., Haarala, S., Lehto, H., et al. 1988, A&A, 203, 1
Valtaoja, E., Lähteenmäki, A., Teräsranta, H., & Lainela, M. 1999, ApJS, 120, 95
Weisstein, E. W. 2005, NP-Hard Problem, MathWorld–A Wolfram Web Resource, http://mathworld.wolfram.com/NP-HardProblem.html
Wills, B. J., Wills, D., Breger, M., Antonucci, R. R. J., & Barvainis, R. 1983, ApJ, 274, 62
Wills, B. J., Wills, D., Breger, M., Antonucci, R. R. J., & Barvainis, R. 1992, ApJ, 398, 454
Woo, J. H., & Urry, C. M. 2002, ApJ, 579, 530
Zensus, J. A., & Pearson, T. J. 1987, JBAA, 98, 48
Zhao, W., Hong, X.-Y., An, T., et al. 2011, A&A, 529, A113